Composites Science and Technology 228 (2022) 109632

Contents lists available at ScienceDirect

Composites Science and Technology

journal homepage: www.elsevier.com/locate/compscitech

Assessment of dynamic mode-I delamination driving force in double cantilever beam tests for fiber-reinforced polymer composite and adhesive materials

Tianyu Chen [a], Yiding Liu [b], Christopher M. Harvey [c,d], Kun Zhang [a,e,*], Simon Wang [c,d], Vadim V. Silberschmidt [f], Bingchen Wei [a,b,g,**], Xiang Zhang [h]

[a] Key Laboratory of Microgravity (National Microgravity Laboratory), Institute of Mechanics, Chinese Academy of Sciences, Beijing, 100190, China
[b] School of Physics, Engineering & Computer Science, University of Hertfordshire, Hatfield, AL10 9AB, UK
[c] Department of Aeronautical and Automotive Engineering, Loughborough University, Loughborough, Leicestershire, LE11 3TU, UK
[d] School of Mechanical and Equipment Engineering, Hebei University of Engineering, Handan, 056038, China
[e] School of Engineering Science, University of Chinese Academy of Sciences, Beijing, 100049, China
[f] Wolfson School of Mechanical, Electrical and Manufacturing Engineering, Loughborough University, Loughborough, Leicestershire, LE11 3TU, UK
[g] Center of Materials Science and Optoelectronics Engineering, University of Chinese Academy of Sciences, Beijing, 100049, China
[h] Centre for Manufacturing and Materials Engineering, Coventry University, Coventry, CV1 5FB, UK

ARTICLE INFO

Keywords:
Double cantilever beam test
Dynamic energy release rate
General displacement loads
Cyclic loads
High loading rate and impact

ABSTRACT

The double cantilever beam (DCB) tests are widely used to assess the interfacial delamination properties of laminated composites. For quasi-static loads, the DCB tests are standardized based on the beam mechanics; for dynamic loads, however, such as high-loading-rate impact and cyclic loads, there is no established analytical theory. This presents a significant obstacle preventing the research community from assessing the delamination behavior of composites or adhesives for their application under complex in-service loads. In this paper, the theory of evaluating dynamic mode-I delamination driving force for DCBs under general displacement loads is developed for the first time, accounting for structural vibration effects. The developed theory is demonstrated by two examples: high-loading-rate split Hopkinson bar impact and cyclic fatigue loads. The analytical solutions are validated by published experiment results and in-house tests. This work provides a fundamental analytical tool to study and assess the fracture behavior of fiber reinforced-polymer composite and adhesive materials under various loading conditions.

1. Introduction

Carbon-fiber-reinforced plastics (CFRPs) are widely used in the aerospace, automotive, civil engineering, energy and other sectors, where the light-weight structures are desired due to their high specific stiffness and strength [1,2]. Without reinforcement in the transverse direction, however, CFRPs are prone to delaminate along the interfaces between laminae [3–5]. Many studies focused on the improvement of fracture toughness by toughening the resins/adhesives [6,7] or by using additional transverse reinforcements (stitching [8,9] or z-pins [10,11]) to improve the delamination-resisting force. To assess the mode-I delamination behavior and to measure the fracture toughness or fatigue delamination growth rate, usually double-cantilever beams (DCBs) are employed according to a standardized test method in ASTM D5528 [12], but this is performed in the quasi-static loading regime. For real engineering structures, however, for instance, aeronautical components, which are prone to impact and in-service cyclic loads, the conventional measurement of delamination driving force, that is, energy release rate (ERR), is not adequate, and further fundamental knowledge of their fracture behavior under dynamic loads is required [13]. It is worth noting that under dynamic and cyclic loads, not only the strain energy can be dissipated during delamination advancement but also the kinetic energy, and, therefore, the delamination driving force is called ERR or

* Corresponding author. Key Laboratory of Microgravity (National Microgravity Laboratory), Institute of Mechanics, Chinese Academy of Sciences, Beijing, 100190, China.
** Corresponding author. Key Laboratory of Microgravity (National Microgravity Laboratory), Institute of Mechanics, Chinese Academy of Sciences, Beijing, 100190, China.
E-mail addresses: chentianyu@imech.ac.cn (T. Chen), zhangkun@imech.ac.cn (K. Zhang), weibc@imech.ac.cn (B. Wei).

https://doi.org/10.1016/j.compscitech.2022.109632
Received 25 January 2022; Received in revised form 27 May 2022; Accepted 6 July 2022
Available online 9 July 2022

Nomenclature

a	Delamination length
c_n	Coefficient of nth polynomial displacement component
d_m	Amplitude of mth cyclic displacement component
E	Young's modulus
f	Frequency of applied cyclic displacement
f_{dyn}	Dynamic factor
$F_n(x)$	Shifting function for nth polynomial displacement component
G	Dynamic energy release rate (ERR) as the total ERR
G_{appl}, G_{dyn}	Applied ERR component, ERR component due to dynamic effect
G_{st}^{U}	ERR component due to the strain energy of quasi-static motion
$H_m(x)$	Shifting function for mth cyclic displacement component
$P(x)$	Shifting function for initial time-independent displacement component
$Q(t)$	Induced displacement
R	Ratio of minimum to maximum applied displacement in cyclic load
$T_i(t)$, $\dot{T}_i(t)$	Modal displacement and velocity of ith normal mode
t	Time
$w_0(t)$	Applied general displacement
w_1	Applied initial time-independent displacement component
$w(x,t)$,$w_{\text{fv}}(x,t)$	Deflections for total and free vibration responses
$W_i(x)$	ith normal mode
β_i	ith vibration mode's wavenumber
δ_{ij}	Kronecker delta
$\delta_{\max}$, $\delta_{\min}$	Applied maximum and minimum cyclic displacement
θ_m	Angular frequency of mth applied cyclic displacement component
ν	Poisson's ratio
ξ_{range}, ξ_{mean}	Contribution of applied range and mean of cyclic displacement
ξ_i	ith induced vibration contribution
ρ	Density
$\varphi_i(x)$	ith mode shape
χ_i	Ratio of ξ_i and ξ_{range}
ω_i	Angular frequency of ith vibration mode

dynamic ERR rather than strain energy release rate [14–17]. As noted by Freund [14], dynamic fracture addresses the fracture phenomena when material inertia becomes significant, and, therefore, the assessment of delamination driving force must consider the inertial effect and kinetic energy associated; this driving force is the dynamic ERR. For a DCB under impact load, the dynamic ERR G as the total ERR can be partitioned into two components, namely, the ERR component due to strain energy of quasi-static motion G_{st}^{U} and the ERR component due to dynamic effect G_{dyn}, where $G = G_{\text{st}}^{\text{U}} + G_{\text{dyn}}$. For a DCB under cyclic load, the dynamic ERR G can be partitioned into two components, namely, the applied ERR component G_{appl} and the ERR component due to dynamic effect G_{dyn}, where $G = G_{\text{appl}} + G_{\text{dyn}}$. This definition is described in Section 2.

The assessment of delamination behavior under impact or high loading rates was initially studied with using a servo-hydraulic machine [18] (with a limited range of high loading rates), and drop weight impact [19] (which suffers from the issue of mixed-mode loading due to unsymmetric opening), and more recently, split Hopkinson bar [20,21]. The last method is more efficient in generation of high-loading rates as well as producing symmetric opening to assess a pure mode-I delamination behavior. But since there is no theory to guide the experimental setup and to post-process the experimental data, the researchers [21–23] had to adopt experimental-numerical methods. Usually, the delamination driving force is calculated with numerical simulations, which require experimental data first, such as the applied displacement or external force, crack length, and, then, incorporate these data into numerical models to derive the ERR with respective numerical methods, such as virtual crack-closure technique (VCCT) or cohesive-zone modelling (CZM). This method lacks transferability that enables one numerical model to be directly adopted to study other cases, since numerical models are mostly suitable for specific cases, so there is a pragmatic requirement for theoretical development to resolve this.

DCBs under cyclic loads can be used to measure fatigue delamination-initiation toughness and study fatigue delamination-propagation behavior. The conventional method standardized in ASTM D6115 [24], allows the fatigue delamination behavior to be tested at frequencies only between 1 and 10 Hz [25,26] to avoid heating effects. Also the solution for the fatigue delamination driving force, that is, maximum strain energy release rate (rather than maximum ERR) accounts only for quasi-static motion, without considering a dynamic effect of cyclic loads. Nevertheless, Maillet et al. [27] designed a novel device capable of applying a frequency of up to 100 Hz with an insignificant temperature rise. For even higher frequencies, heating effects can be mitigated by cooling [28] or intermittently interrupted cooling [29]. The assessment of the fatigue delamination driving force in ASTM D6115 [24], however, still requires measurement of the applied load, but under high-frequency cyclic loads, the slender DCB structure experiences significant vibration due to inertia. In this case, therefore, the external force cannot be measured accurately, resulting in an incorrect assessment of dynamic ERR. To address this, an analytical theory considering the dynamic effect of DCB but allowing no measurement of external force is desirable, which can be used to investigate the cyclic-load-induced dynamic effect as well as the frequency effect for fatigue delamination driving force.

As discussed above, the previous literature was focused more on experimental analysis using experiments at high-loading-rate, impact and cyclic loads. To the authors' best knowledge, no analytical model was developed to study the dynamic effect explicitly; therefore, researchers have to resort to experimental-numerical methods. Accordingly, in this paper, the theory of dynamic mode-I delamination in a DCB test is developed for general displacement loads including high-loading-rate and cyclic ones to provide an analytical solution that can be employed to study the dynamic effect and to post-process the experimental data for delamination initiation. The theoretical solutions for the delamination driving force in presence of structural vibration would allow measurements of the dynamic fracture toughness at initiation under arbitrary dynamic loads as well as investigations of fatigue delamination behavior. Note that the delamination propagation under dynamic loads, as a dynamic moving boundary problem, is beyond the scope of this paper, since it requires consideration of crack-propagating speeds, the dispersive nature of the beam as 1D waveguide to supply the energy flux to the crack tip, and the Doppler effect due to the fast-moving crack tip. The interested readers can consider [16]. In this paper, the theory is derived in Section 2 and applied to delamination problems under split Hopkinson bar impact and cyclic loads. Validation by experiments and verification against numerical models are presented in Section 3. Conclusions are given in Section 4.

2. Theory

In this section, a theoretical solution for the dynamic ERR of a DCB

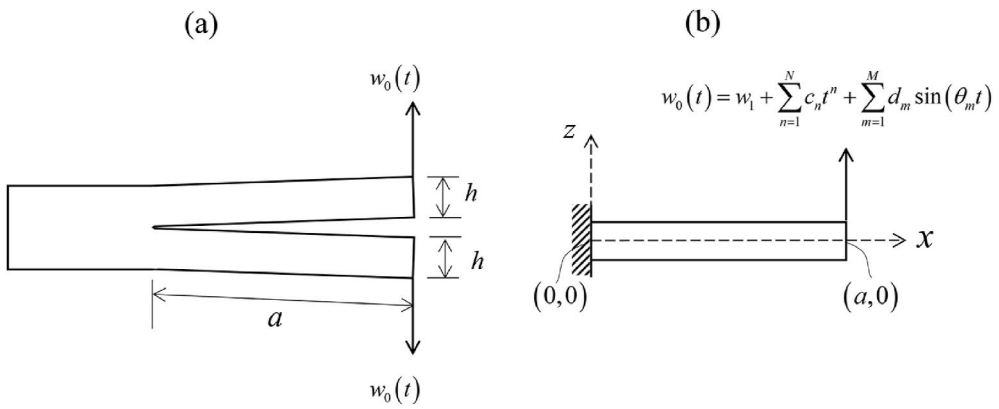

Fig. 1. (a) Schematic of DCB specimen; (b) prescribed coordinate system and boundary assumption.

specimen under general displacement loads (as the loading conditions) is derived analytically in the context of structural vibration based on beam dynamics. The configuration of the symmetric DCB specimen is shown in Fig. 1a: the delamination length is a, the thickness and width for one DCB arm are h and b, and, therefore, the cross-sectional area is $A = bh$ and the second moment of area is $I = bh^3/12$. Following the conventional analytical method of analyzing a DCB, the delaminated region of the beam is isolated and assigned the coordinates as shown in Fig. 1b, where the crack tip is assumed to be built-in at $x = 0$, with the deflection of beam section in x-z plane, denoted $w(x,t)$. Note that in reality the crack tip can rotate, and so the built-in boundary-condition assumption does not predict the ERR accurately. This is addressed by introducing the effective delamination length $a_{\text{eff}} = (a + \Delta)$, as in ASTM D5528 [12] originating in Ref. [30], or by analytical solution [31]. It is also assumed that $h \ll a$, so that the Euler-Bernoulli beam theory applies.

The general applied time-dependent displacement at the free end is assumed to be of the form

$$w_0(t) = w_1 + \sum_{n=1}^{N} c_n t^n + \sum_{m=1}^{M} d_m \sin(\theta_m t) \,, \tag{1}$$

where w_1 is the initial time-independent displacement component, $\sum_{n=1}^{N} c_n t^n$ is the time-dependent polynomial component, and $\sum_{m=1}^{M} d_m \sin(\theta_m t)$ is the harmonic component, representing quasi-static, dynamic and cyclic applied displacements, respectively.

Generally, the ERR of a stationary delamination in a DCB under dynamic loads can be determined by the crack-tip bending moments, using a crack-tip energy flux integral [14,16], and the dynamic ERR is

$$G = 2\frac{1}{2bE}\frac{\left[EIw^{(2)}(0,t)\right]^2}{I} \,, \tag{2}$$

where $EIw^{(2)}(0,t)$ is the internal bending moment of one DCB arm at crack tip $x = 0$, with $w(x,t)$ being the displacement of this DCB arm (Fig. 1b), and the coefficient of 2 in Eq. (2) indicates that the total ERR is for DCB specimen with two DCB arms. Eq. (2) is for the plane-stress condition. For the plane-strain condition, E in Eq. (2) and throughout this paper should be replaced with $E/(1 - \nu^2)$.

The deflection of the DCB arm shown in Fig. 1b is derived in Section 2.1, which is then employed to determine the dynamic ERR in Section 2.2 with two important applications for a split Hopkinson bar impact in Section 2.2.1 and for a cyclic fatigue load in Section 2.2.2.

2.1. Dynamic transverse response of DCB arm under general displacement

2.1.1. Deflection assumptions

Under the applied general displacement $w_0(t)$ given in Eq. (1), the dynamic transverse deflections of the DCB arm $w(x,t)$ can be assumed of the following form by introducing shifting functions [32]:

$$w(x,t) = P(x)w_1 + w_{\text{fv}}(x,t) + F_0(x) + \sum_{n=1}^{N} F_n(x)c_n t^n + \sum_{m=1}^{M} H_m(x)d_m \sin(\theta_m t) \,, \tag{3}$$

where $P(x)$ is the shifting function for the time-independent initial displacement of w_1, $w_{\text{fv}}(x,t)$ is the free-vibration component, and $F_n(x)$ and $H_m(x)$ are the corresponding shifting functions for applied polynomial-displacement and harmonic-displacement components, respectively. The physical understanding of shifting functions is the distribution of the respective applied displacement components along the DCB arm. Particularly for the quasi-static component w_1, it is not time-dependent and, therefore, its contribution can be solved within the quasi-static beam mechanics giving $P(x) = -x^3/(2a^3) + 3x^2/(2a^2)$. The 0th-order shifting function $F_0(x)$ is time-independent but induced by the time-dependent polynomial displacement component according to Grant [32], indicating the nonlinear effects of the applied polynomial-displacement component.

The governing equations for the free-vibration component $w_{\text{fv}}(x,t)$, and the shifting functions $F_n(x)$ and $H_m(x)$, are now derived (boundary conditions detailed in Appendix A). It is worth noting that the boundary conditions for the 0th shifting function are $F_0(a) = 0$, different from the other order shifting functions, for which $F_n(a) = 1$ $(n \geq 1)$. The free-vibration solution for $w_{\text{fv}}(x,t)$ is given in Section 2.1.2 and the solutions for the shifting functions $F_n(x)$ and $H_m(x)$ are in Sections 2.1.3 and 2.1.4, respectively.

The equation of motion for the Euler-Bernoulli beam [33] in free vibration is

$$EIw^{(4)}(x,t) + \rho A\ddot{w}(x,t) = 0 \,. \tag{4}$$

By combining Eqs. (3) and (4), and forcing homogeneous conditions, the governing equations for the free-vibration component and the shifting functions are derived as

$$EIw_{\text{fv}}^{(4)}(x,t) + \rho A\ddot{w}_{\text{fv}}(x,t) = 0 \,, \tag{5}$$

$$EI\sum_{n=1}^{N} F_n^{(4)}(x)c_n t^n + \rho A\sum_{n=2}^{N} n(n-1)F_n(x)c_n t^{n-2} = 0 \,, \tag{6}$$

$$EI\sum_{m=1}^{M} H_m^{(4)}(x) - \rho A\sum_{m=1}^{M} \theta_m^2 H_m(x) = 0 \,. \tag{7}$$

2.1.2. Solution for free-vibration component

By the method of separation of variables, the free-vibration component $w_{\text{fv}}(x,t)$ can be expressed as a summation of products of normal mode $W_i(x)$ and modal displacement $T_i(t)$:

$$w_{\mathrm{fv}}(x,t)=\sum_{i=1}^{\infty}W_i(x)T_i(t)\ . \tag{8}$$

The solution for the normal mode [15,34] is

$$W_i(x)=\sqrt{1/(\rho Aa)}\varphi_i(x)\ , \tag{9}$$

where $\varphi_i(x)$ is the mode shape given as

$$\varphi_i(x)=\cosh(\beta_i x)-\cos(\beta_i x)-\sigma_i[\sinh(\beta_i x)-\sin(\beta_i x)]\ . \tag{10}$$

In Eq. (10), β_i is the wavenumber, obtained by $\tan(\lambda_i)-\tanh(\lambda_i)=0$ (frequency equation) with $\lambda_i=\beta_i a$; and $\sigma_i=[\cosh(\lambda_i)-\cos(\lambda_i)]/[\sinh(\lambda_i)-\sin(\lambda_i)]$. The solution for the frequency equation λ_i and the value for σ_i are given in Appendix B.

As for the modal displacement $T_i(t)$, its governing equation is obtained by combining Eqs. (4) and (8) and introducing the ith mode's natural frequency $\omega_i=\beta_i^2\sqrt{EI/(\rho A)}$ as

$$T_i(t)=T_i(0)\cos(\omega_i t)+\frac{\dot{T}_i(0)}{\omega_i}\sin(\omega_i t)\ , \tag{11}$$

where $T_i(0)$ and $\dot{T}_i(0)$ are the initial modal displacement and velocity, respectively. According to Ref. [33], they can be determined from the initial displacement $w_{\mathrm{fv}}(x,0)$ and the velocity $\dot{w}_{\mathrm{fv}}(x,0)$ of the free-vibration component, respectively, as

$$T_i(0)=\int_0^a \rho A W_i(x)w_{\mathrm{fv}}(x,0)dx\ , \tag{12}$$

$$\dot{T}_i(0)=\int_0^a \rho A W_i(x)\dot{w}_{\mathrm{fv}}(x,0)dx\ . \tag{13}$$

In Eq. (1), by setting $t=0$ with $w(x,0)=w_1P(x)$ and $\dot{w}(x,0)=0$, the initial displacement and velocity of free vibration are found to be

$$w(x,t)=\frac{1}{a}\sum_{i=1}^{\infty}\varphi_i(x)\left\{\begin{array}{l}-\int_0^a\varphi_i(x)F_0(x)dx\cos(\omega_i t)\\ +\frac{1}{\omega_i}\left[-c_1\int_0^a\varphi_i(x)F_1(x)dx+\beta_i^3\Lambda_i\sum_{m=1}^{M}\frac{\theta_m d_m}{(\beta_i^4-\gamma_m^4)}\right]\sin(\omega_i t)\end{array}\right\}$$
$$+P(x)w_1+F_0(x)+\sum_{n=1}^{N}F_n(x)c_n t^n+\sum_{m=1}^{M}H_m(x)d_m\sin(\theta_m t)\ , \tag{20}$$

$$w_{\mathrm{fv}}(x,0)=-F_0(x)\ , \tag{14}$$

$$\dot{w}_{\mathrm{fv}}(x,0)=-c_1F_1(x)-\sum_{m=1}^{M}d_m\theta_m H_m(x)\ . \tag{15}$$

Note that determination of $T_i(0)$ and $\dot{T}_i(0)$ via Eqs. (12)–(15) requires the solutions for shifting functions $F_n(x)$ and $H_m(x)$ (given in Sections 2.1.3 and 2.1.4).

2.1.3. Solutions for shifting functions for polynomials

The shifting functions for $F_n(x)$ by solving the ordinary differential equation Eq. (6) together with the available boundary conditions (Appendix A). Examination of Eq. (6) reveals $F_N^{(4)}(x)=0$, $F_{N-1}^{(4)}(x)=0$, and $EIF_{n-2}^{(4)}(x)c_{n-2}+\rho An(n-1)F_n(x)c_n=0$ for $2\le n\le N-2$ ($c_0=1$). Therefore, the solutions for $F_{N-1}^{(4)}(x)$ and $F_N^{(4)}(x)$ are

$$F_N(x)=-\frac{1}{2a^3}x^3+\frac{3}{2a^2}x^2\ , \tag{16}$$

$$F_{N-1}(x)=-\frac{1}{2a^3}x^3+\frac{3}{2a^2}x^2\ . \tag{17}$$

And for $F_n(x)$ ($2\le n\le N-2$) can be obtained by solving Eq. (6) iteratively.

For the case of $N=3$, for instance, the solutions of the shifting functions for the applied polynomial-displacement component are

$$\left\{\begin{array}{l}F_3(x)=F_2(x)=-\frac{1}{2a^3}x^3+\frac{3}{2a^2}x^2\ ,\\ F_1(x)=-\frac{1}{1680a^3}\left[k_1x^7-7k_1ax^6+\left(39k_1a^4+840\right)x^3-\left(33k_1a^5+2520a\right)x^2\right]\ ,\\ F_0(x)=-\frac{k_0}{1680a^3}\left(x^7-7ax^6+39a^4x^3-33a^5x^2\right)\ ,\end{array}\right. \tag{18}$$

where $k_1=-6c_3\rho A/(c_1EI)$ and $k_0=-2c_2\rho A/(c_0EI)$. The solutions for $N=1$, $N=2$ and $N=4$ are given in Supplementary file.

2.1.4. Solutions for shifting functions for harmonics

The shifting functions for $H_m(x)$ are obtained by solving the differential equation Eq. (7) together with the boundary conditions (Appendix A).

$$H_m(x)=\frac{[\sin(\gamma_m a)+\sinh(\gamma_m a)]}{2[\cos(\gamma_m a)\sinh(\gamma_m a)-\cosh(\gamma_m a)\sin(\gamma_m a)]}$$
$$\left\{-\cosh(\gamma_m x)+\cos(\gamma_m x)+\frac{\cos(\gamma_m a)+\cosh(\gamma_m a)}{\sin(\gamma_m a)+\sinh(\gamma_m a)}[\sinh(\gamma_m x)-\sin(\gamma_m x)]\right\}\ , \tag{19}$$

where $\gamma_m^4=\theta_m^2\rho A/(EI)$.

The combined results from Sections 2.1.1 to 2.1.4 give the deflection of the DCB arm (shown in Fig. 1b) in Eq. (3) as

where $\Lambda_i=[(-1)^i\sqrt{\sigma_i^2+1}+\sqrt{\sigma_i^2-1}\,]$ (values given in Appendix B). The derivation of the integral $\int_0^a\varphi_i(x)H_m(x)dx$, $\int_0^a\varphi_i(x)F_0(x)dx$ and $\int_0^a\varphi_i(x)F_1(x)dx$ are by partial integration (details in Supplementary file).

As shown in Eq. (20), the total deflection is a combination of the free-vibration component and extrapolations of the other general applied displacement components. For the applied polynomial-displacement component, the 0th-order shifting function $F_0(x)$ affects the initial modal displacement of the free-vibration, while the first-order shifting function $F_1(x)$ affects the modal velocity; still, the other remaining shifting functions do not affect the free-vibration component. For the applied harmonic-displacement component, its associated shifting functions $H_m(x)$ do not affect the modal displacement but affect the modal velocity.

2.2. Energy release rate

By combining Eqs. (2) and (20), the total dynamic ERR for the DCB specimen shown in Fig. 1 is obtained as

$$G=\frac{EI}{b}\left\{\begin{array}{l}\frac{2}{a}\sum_{i=1}^{\infty}\left[\begin{array}{l}-\beta_i^2\int_0^a\varphi_i(x)F_0(x)dx\cos(\omega_i t)\\-\frac{c_1\beta_i^2}{\omega_i}\int_0^a\varphi_i(x)F_1(x)dx\sin(\omega_i t)\\+\frac{\beta_i^5\Lambda_i}{\omega_i}\sum_{m=1}^{M}\frac{\theta_m d_m}{(\beta_i^4-\gamma_m^4)}\sin(\omega_i t)\end{array}\right]+\frac{3}{a^2}w_1\\+F_0^{(2)}(0)+\sum_{n=1}^{N}F_n^{(2)}(0)c_n t^n-\sum_{m=1}^{M}\frac{\gamma_m^2 d_m[\sinh(\gamma_m a)+\sin(\gamma_m a)]}{[\sinh(\gamma_m a)\cos(\gamma_m a)-\cosh(\gamma_m a)\sin(\gamma_m a)]}\sin(\theta_m t)\end{array}\right\}^2. \tag{21}$$

Note that Eq. (21) is for the general applied displacement with a combination of quasi-static, polynomial and harmonic components; pragmatically, for a specific DCB test, the applied displacement might be a component of $w_0(t)$ in Eq. (1). For instance, under impact loads, the displacement can be only polynomials. Under cyclic loads (conventional fatigue test) can only be a combination of quasi-static displacement component determining the mean stress level and one harmonic component determining the stress amplitude. Therefore, these two immediate applications are investigated in detail in Section 2.2.1 for impact and in Section 2.2.2 for fatigue.

2.2.1. ERR solution for DCB under impact loads

Generally, the displacement at the free end of one DCB arm under impact loads, such as drop weight or split Hopkinson bar, can be obtained with a high-speed camera or by measuring of the incident and reflected strain waves [21]. Once this displacement is obtained, it can be fitted into polynomials, and by resorting to Eq. (21), the ERR can be determined.

Assuming that the impact loads are applied to the undeformed DCB with a zero initial displacement, that is, $w_1 = 0$ in Eq. (1), and free-end displacement of one DCB arm can be fitted into the 3rd order-polynomial, i.e. $N = 3$ as a case of Eq. (1):

$$w_0(t)=c_1 t+c_2 t^2+c_3 t^3\ . \tag{22}$$

Then, by substituting Eqs. (18) and (22) into the general solution (Eq. (21)), and by regrouping the relevant terms, the dynamic ERR is then

$$G=\frac{9EI}{ba^4}[w_0(t)+Q(t)]^2\ , \tag{23}$$

where $Q(t)$ is induced displacement by the structural dynamic response:

$$\begin{aligned}Q(t)=&-\frac{4}{3}c_2 a^4\frac{\rho A}{EI}\sum_{i=1}^{\infty}\frac{\Lambda_i}{\lambda_i^3}\cos(\omega_i t)+\frac{2}{3}c_1 a^2\sqrt{\frac{\rho A}{EI}}\sum_{i=1}^{\infty}\frac{\Lambda_i}{\lambda_i}\sin(\omega_i t)\\&-4c_3 a^6\frac{\rho A}{EI}\sqrt{\frac{\rho A}{EI}}\sum_{i=1}^{\infty}\frac{\Lambda_i}{\lambda_i^5}\sin(\omega_i t)-\frac{11}{420}c_2 a^4\frac{\rho A}{EI}-\frac{11}{140}c_3 a^4\frac{\rho A}{EI}t\ .\end{aligned} \tag{24}$$

Note that when determining the dynamic ERR in Eq. (23), the total response of one DCB arm is considered, which includes the applied displacement $w_0(t)$ and induced displacement $Q(t)$ due to structural vibration caused by the inertial effect. Also note that the total ERR in Eq. (23) includes the ERR components from the applied displacement $w_0(t)$ and the induced displacement $Q(t)$ as well as their coupling. The quasi-static component of the ERR (or strain ERR) can be determined by using the applied displacement $w_0(t)$ directly in the quasi-static solution for the DCB, which gives the ERR component of quasi-static motion as

$$G_{\rm st}^{\rm U}=\frac{9EIw_0^2(t)}{ba^4}. \tag{25}$$

Therefore, the total ERR in Eq. (23) can be written as a sum of quasi-static ERR $G_{\rm st}^{\rm U}$ and dynamic ERR components $G_{\rm dyn}$ as

$$G=G_{\rm st}^{\rm U}+G_{\rm dyn}\ , \tag{26}$$

where

$$G_{\rm dyn}=\frac{9EI}{ba^4}\left[2w_0(t)Q(t)+Q^2(t)\right]\ , \tag{27}$$

and, therefore, the dynamic factor can be defined as

$$f_{\rm dyn}=\frac{G_{\rm dyn}}{G_{\rm st}^{\rm U}}=2\frac{Q(t)}{w_0(t)}+\left[\frac{Q(t)}{w_0(t)}\right]^2. \tag{28}$$

Note that Eq. (27) represents all the dynamic effects, that is, the induced displacement and its coupling with the applied displacement. Specifically, these dynamic effects are: (1) inertia-induced local vibration, represented by terms with $\sin(\omega_i t)$, and (2) coupling between the local vibration and applied displacement, represented by terms with the product of $w_0(t)\sin(\omega_i t)$. However, in Eq. (24), interestingly, there are two terms of $-11\rho A c_2 a^4/(420EI)$ and $-11c_3 a^4\rho A t/(140EI)$ not related to the above two sources, and the close examination shows that they come from the shifting function $F_1(x)$, which is solved by Eq. (6) that the solution of $F_1(x)$ depends on the solution of $F_3(x)$. This shows a nonlinear relationship between shifting $F_n(x)$ and the solutions for $F_n(x)$ causes the motion coupling of the applied displacement when the ERR is determined. And, therefore, this identifies the third dynamic-effect source, which is the motion coupling of the applied polynomial displacement itself.

It is also worth noting that for the applied displacement of form $w_0(t) = vt$ (setting $c_1 = v$ being the constant opening rate), that is, the DCB under constant high loading rate, the ERR is

$$G=\frac{9EIv^2t^2}{ba^4}+\frac{12\sqrt{\rho AEI}v^2t}{ba^2}\sum_{i=1}^{\infty}\frac{\Lambda_i}{\lambda_i}\sin(\omega_i t)+\frac{4\rho Av^2}{b}\left[\sum_{i=1}^{\infty}\frac{\Lambda_i}{\lambda_i}\sin(\omega_i t)\right]^2, \tag{29}$$

which coincides with [16].

2.2.2. ERR solution for DCB under cyclic loads

The general solution for the ERR in Eq. (21) can also be applied to investigate the fatigue delamination under cyclic loads. Following the conventional method in ASTM D6115 [24], that is, applying a cyclic displacement with the maximum value $\delta_{\max}$ and the minimum value $\delta_{\min}$, the applied displacement is

$$w_0(t)=w_1+d\sin(\theta t)\ , \tag{30}$$

where $w_1=(\delta_{\max}+\delta_{\min})/2$ is the half mean applied amplitude, $d=(\delta_{\max}-\delta_{\min})/2$ is the half range or amplitude, $\theta=2\pi f$ is the angular frequency with f being the applied frequency. Note that $\delta_{\max}$ and $\delta_{\min}$ are for one DCB arm measured from the symmetry line. Taking these into Eq. (21), the ERR for this fatigue cyclic displacement load is

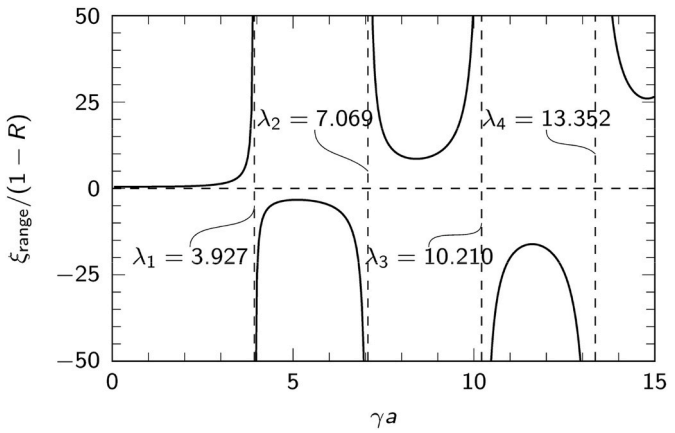

Fig. 2. Contribution to total ERR from applied cyclic loads.

$$G = \frac{9EI\delta_{\max}^2}{ba^4}\left[\xi_{\text{mean}} + \xi_{\text{range}}\sin(\theta t) + \sum_{i=1}^{\infty}\xi_i \sin(\omega_i t)\right]^2, \tag{31}$$

where

$$\xi_{\text{mean}} = \frac{1}{2}(1+R), \tag{32}$$

$$\xi_{\text{range}} = -\frac{1}{6}(1-R)\frac{\gamma^2 a^2[\sinh(\gamma a)+\sin(\gamma a)]}{[\sinh(\gamma a)\cos(\gamma a)-\cosh(\gamma a)\sin(\gamma a)]}, \tag{33}$$

$$\xi_i = \frac{1}{3}(1-R)\frac{\lambda_i^3 \Lambda_i \gamma^2 a^2}{(\lambda_i^4 - \gamma^4 a^4)}, \tag{34}$$

are the contributions to the total ERR from the mean load, the load range and the ith induced vibration, respectively, with $R = \delta_{\min}/\delta_{\max}$ being the cyclic load ratio.

Note that the advantages of Eq. (31) allow to determine the fatigue delamination driving force, i.e. $G_{\max}$ under the maximum load, without the need of measuring the applied loads as required by ASTM D6115. This is especially significant for high-frequency cyclic displacements, where the applied loads oscillate considerably and are very hard to measure.

A close examination of $\xi_{\text{range}}/(1-R)$ and $\xi_i/(1-R)$ reveals that they are both dimensionless and functions only of dimensionless parameter γa (note that γ represents the applied frequency and structural property for $\gamma^4 = 4\pi^2 f^2 \rho A/(EI)$). They are plotted versus γa in Figs. 2 and 3 to illustrate their properties.

It is seen that the values of $\xi_{\text{range}}/(1-R)$ and $\xi_i/(1-R)$ remain relatively small when γa is not in the vicinity of the eigenvalues λ_i; otherwise, the beam system would go resonant giving an infinite value for ERR as the material fails immediately.

Note that the induced vibration contributions ξ_i are from the applied cyclic displacement range ξ_{range}, and, therefore, it is important to investigate the ratio between them to demonstrate the contribution from the applied cyclic displacement to the induced vibration as the relative dynamic effect. χ_i is defined as

$$\chi_i = \frac{\xi_i}{\xi_{\text{range}}} = -\frac{2\lambda_i^3 \Lambda_i[\sinh(\gamma a)\cos(\gamma a) - \cosh(\gamma a)\sin(\gamma a)]}{(\lambda_i^4 - \gamma^4 a^4)[\sinh(\gamma a) + \sin(\gamma a)]}. \tag{35}$$

Fig. 4 shows the relationship between ξ_i and ξ_{range} for a range of γa values. For the first vibration mode, χ_1 increases with γa to a peak value of approximate 1.4, demonstrating the maximum dynamic response is $\xi_1 = 1.4\xi_{\text{range}}$; then χ_1 drops steadily to zero. However, the interpretation of this should be based on the real composite material, considering a less stiff CFRP with the longitudinal modulus of 10 GPa, density of 1000 kg m^{-3}, and DCB with $h = 1.5$ mm and $a = 125$ mm (limiting geometry in ASTM D5528), the applied frequency of 100 Hz, which gives $\gamma a = a\sqrt[4]{4\pi^2 f^2 \rho A/(EI)} = 2.67$; to increase the applied frequency further seems impossible due to the limitation of available experimental systems [27]. Therefore, in a realistic case, the value of γa might be well below 5, where the relative dynamic factor χ_i decreases with increasing vibration-mode number, and the first vibration mode makes the largest

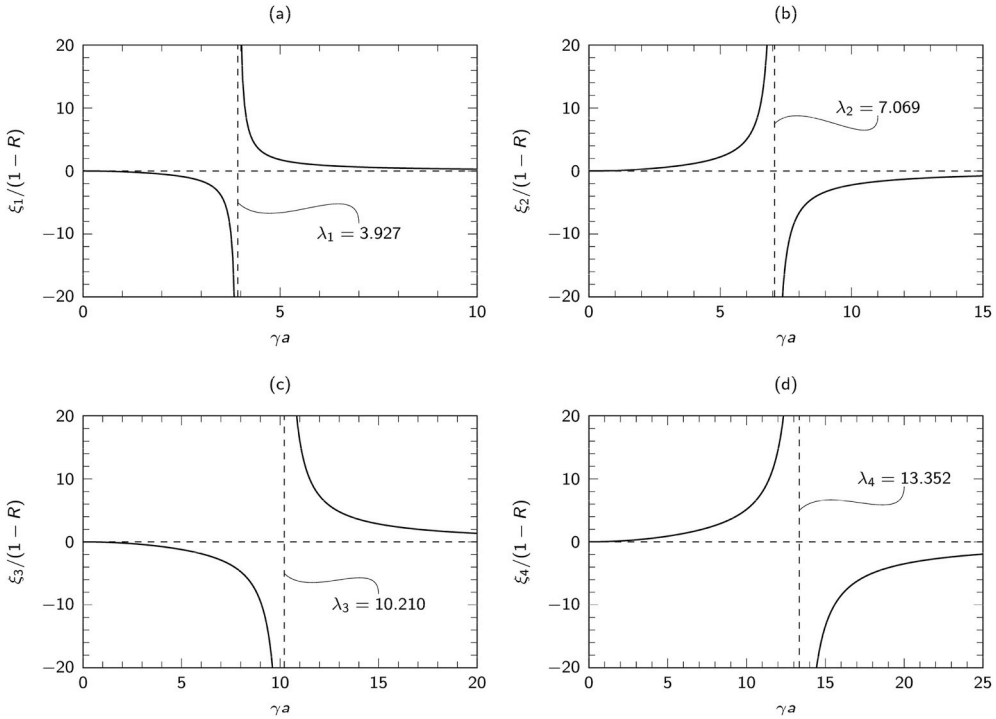

Fig. 3. Contribution to total ERR from ith induced free vibration.

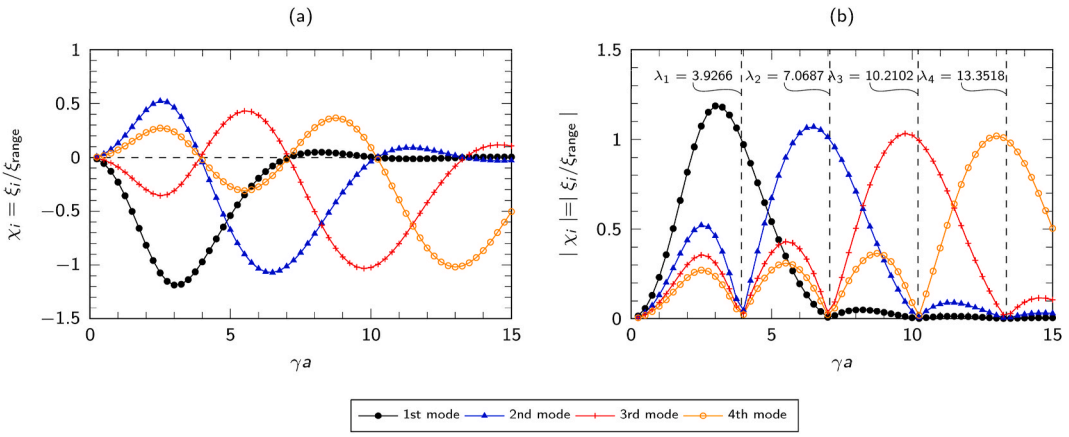

Fig. 4. (a) Vibration-induced dynamic factors; (b) absolute value of vibration-induced dynamic factors.

contribution compared with those of other vibration modes.

Another approach to study the induced dynamic contribution to the total ERR is by investigating the absolute values, that is, the applied ERR component G_{appl} and vibration induced ERR component G_{dyn} by expanding the Eq. (31) to have

$$G = G_{appl} + G_{dyn}\ , \tag{36}$$

where

$$G_{appl} = \frac{9EI\delta_{max}^2}{ba^4}\left[\xi_{mean} + \xi_{range}\sin(\theta t)\right]^2\ , \tag{37}$$

$$G_{dyn} = \frac{9EI\delta_{max}^2}{ba^4}\left\{2\left[\xi_{mean} + \xi_{range}\sin(\theta t)\right]\sum_{i=1}^{\infty}\xi_i\sin(\omega_i t) + \left[\sum_{i=1}^{\infty}\xi_i\sin(\omega_i t)\right]^2\right\}, \tag{38}$$

and, therefore, the dynamic factor can be defined as

$$f_{dyn} = \frac{G_{dyn}}{G_{appl}} = \frac{2\left[\xi_{mean} + \xi_{range}\sin(\theta t)\right]\sum_{i=1}^{\infty}\xi_i\sin(\omega_i t) + \left[\sum_{i=1}^{\infty}\xi_i\sin(\omega_i t)\right]^2}{\left[\xi_{mean} + \xi_{range}\sin(\theta t)\right]^2}\ . \tag{39}$$

Note that Eqs. (31)–(39) are for the ERR time response: for its application to study fatigue delamination initiation and propagation, the range or the maximum value of the ERR should be used, and they are denoted G_{max}, $G_{appl,max}$ and $G_{dyn,max}$, respectively, for the maximum value of Eqs. (36)–(38).

3. Applications and verifications

3.1. DCB under split Hopkinson bar impact

To demonstrate and to verify the applications of the developed theory for impact, the experimental data of the DCB of unidirectional

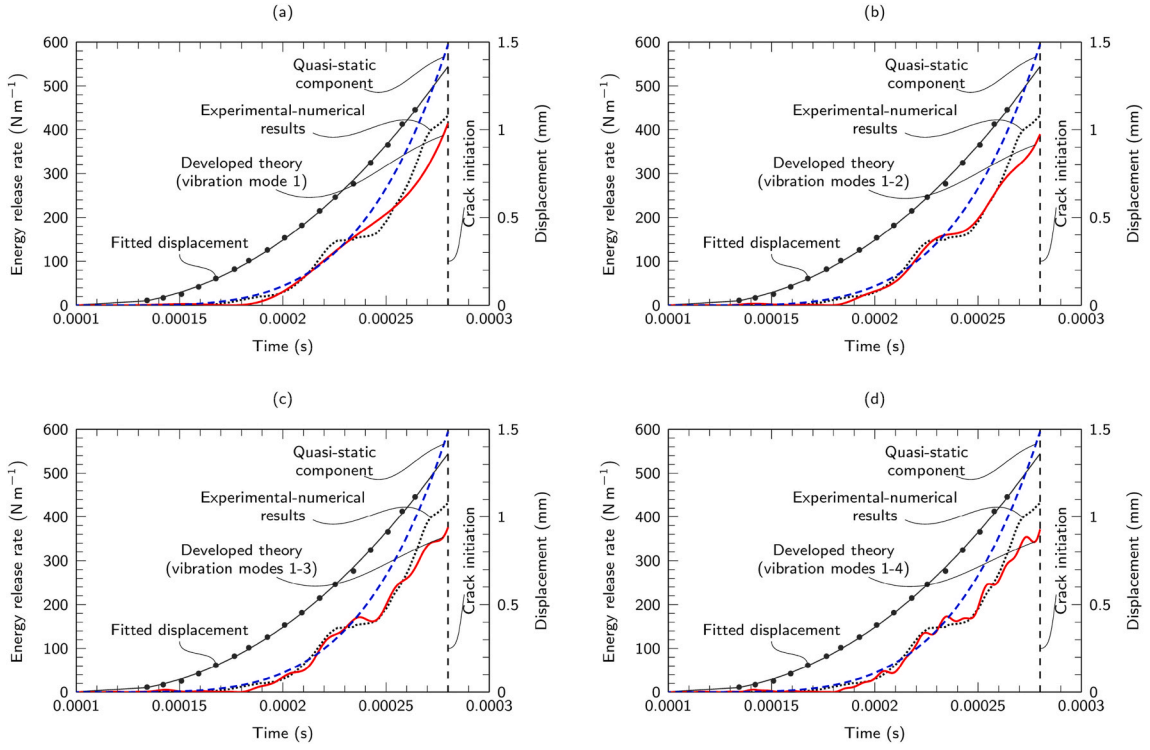

Fig. 5. Dynamic ERR versus time results from developed theory with first (a), first two (b), first three (c), and first four (d) vibration modes together with dynamic ERR data from experimental-numerical results for CFRP specimens of unidirectional stacking sequence.

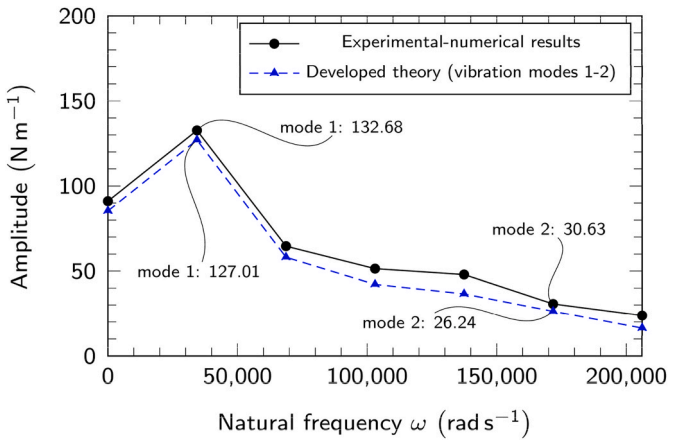

Fig. 6. Comparison of FFT results for experimental-numerical method and developed theory for first two vibration modes.

CFRP specimens manufactured from the T700/MTM28-1 prepreg in the split Hopkinson bar impact test from Ref. [21] is used. The displacement curve was adopted from Ref. [21] and fitted into a third-order displacement curve:

$$w_0(t) = 2.625 \times 10^{10}(t - t_0)^3 + 4.065 \times 10^7(t - t_0)^2 - 7.885 \times 10^2(t - t_0) \quad R^2 = 0.999\ , \tag{40}$$

where $t_0 = 9.8 \times 10^{-5}$ s is the estimated time for the DCB arm to start to deflect at the arrival of incident wave as shown in Fig. 5a in Ref. [21].

Then it was substituted in Eq. (23) to determine the dynamic ERR G that is compared with experimental-numerical solution from Ref. [21] in Fig. 5 for a number of different vibration modes.

Fig. 5 shows an excellent agreement between the analytical solution and the experimental-numerical results until crack-initiation time determined experimentally in Ref. [21] and the analytical solution captures the oscillating nature of the ERR. The analytical solution with the first vibration mode gives a mean value of the total ERR as shown in Fig. 5a. By adding the second vibration mode (Fig. 5b), the analytical solution approaches the experimental-numerical results. With addition of the third (Fig. 5c) and fourth (Fig. 5d) vibration modes, the analytical solution becomes more oscillatory around the mean value of the first vibration mode. This may be due to different formations: the analytical solution is based on the 1D plane-strain condition using a longitudinal modulus, whereas the experimental-numerical result was derived from a 2D finite-element-method (FEM) simulation with an orthotropic material properties [21]. Still, the difference between the analytical solution and the experimental-numerical result is insignificant. Note that the value of the dynamic ERR G is very small at the initial stage at the arrival of incident wave, and before 0.00018 s, the G value approaches to zero while the quasi-static component $G_{\mathrm{st}}^{\mathrm{U}}$ increases with time. This is due to the negative effect of ERR component due to dynamic effect G_{dyn}, which is further examined in Fig. 7.

The agreement between the prediction of the developed theory and experimental-numerical results can also be demonstrated with the Fast Fourier Transform (FFT) that provides a quantitative assessment (Fig. 6). According to this, the contribution of the first vibration mode in experimental-numerical results is 132.68 N m^{-1}, while the respective theoretical result is 127.01 N m^{-1}, with the error of −4.27%; for the second vibration mode, this error is −14.33%.

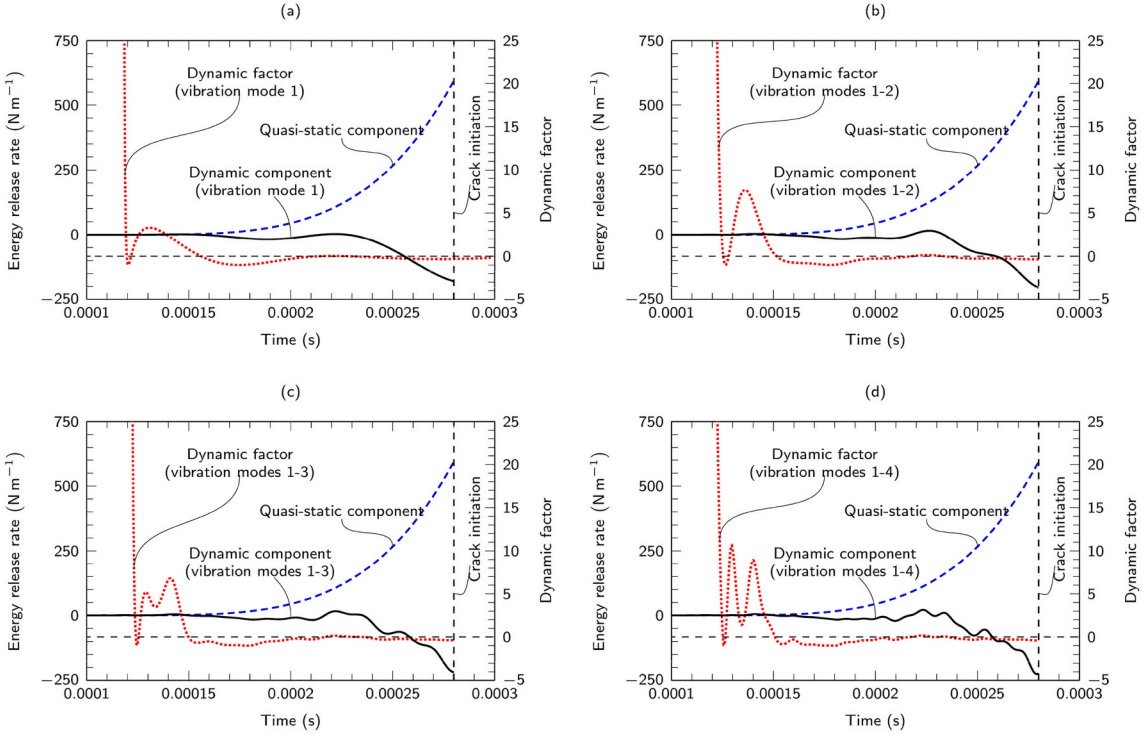

Fig. 7. Time response of dynamic ERR components and corresponding dynamic factors for first (a), first two (b), first three (c) and first four (d) vibration modes.

It is worth noting that the quasi-static solution is also plotted in Fig. 7 for comparison, and it seems that the dynamic effect lowered the total ERR and postponed the crack initiation. To further investigate the process, the ERR's quasi-static component G_{st}^{U} (Eq. (25)), dynamic component G_{dyn} (Eq. (26)) and dynamic factor f_{dyn} (Eq. (27)) were plotted (Fig. 7). Note that the ERR component due to quasi-static motion G_{st}^{U} is also referred as the strain energy release rate that can be calculated with a conventional data-reduction method when dynamic effect is not considered. The comparison between G_{st}^{U} and dynamic ERR G presented in this study (Figs. 5 and 7) also demonstrates the significance of the dynamic effect.

It is seen in Fig. 7 that the G_{dyn} actually increases initially and then decreases with time; and this is due to the crack-tip motion that after the immediate impact the deflection around the crack tip experiences an additional opening tendency giving positive G_{dyn} and f_{dyn}. After that, due to the structural vibration and the associated reciprocating motion, the crack tip undergoes closing and reduces the total ERR, resulting in negative G_{dyn} and f_{dyn}.

In general, the developed theory and the associated analytical solution for the split Hopkinson bar impact provides an accurate prediction of the delamination driving force compared with experimental-numerical methods, making it a powerful analytical tool to further study the dynamic effect accompanied by the structural vibration, which the experimental-numerical methods cannot achieve.

3.2. DCB under cyclic loads

3.2.1. Experimental verification

To confirm the applicability of the developed theory for fatigue delamination, in-house fatigue experiments were conducted in accordance with ASTM D6115 (Fig. 8a) for specimens with a width of 20 mm. Each cantilever beam was made of 16 plies of Hexply 8552/AS7 (density: 1790 kg m^{-3}) CFRP in a quasi-isotropic layup of $[0/45/90/-45]_{2s}$, giving a thickness $h = 2.2$ mm. Two beams were bonded with FM94 adhesive. The elastic properties of the laminate and the adhesive are given in Table 1. To monitor the delamination length, one side of the specimen was painted with white spray and marked with a vernier height gauge at 1 mm interval (Fig. 8b).

Table 1
Elastic properties of laminate and adhesives used in DCB specimens.

Material	E_1 (GPa)	E_2 (GPa)	G_{12} (GPa)	ν_{12}
8552/AS7 laminate	56.42	56.42	21.64	0.30
FM94 adhesive	3	3	1.15	0.35

An Instron 8841 fatigue test machine (Fig. 8c) was used to provide displacement control with the maximum displacement $\delta_{max} = 2.3$ mm, $R = 0.1$ and $f = 5$ Hz. The applied loads were measured and the maximum value P_{max} for each delamination length is recorded. The delamination length was measured when the test was paused at the maximum displacement. According to ASTM D6115, the maximum ERR can be calculated via expression $G_{max} = (3P_{max}\delta_{max})/[b(a+\Delta)]$ (where δ_{max} is for one DCB arm). This experimentally determined maximum ERR value, G_{max}, is then compared with the theoretical solution (Eq. (31)) for various delamination lengths in Fig. 9.

Fig. 9 shows that the analytical solution and experimental result are in excellent agreement, but the analytical solution does not require the measurement of the applied load. To study the influence of the vibration-induced dynamic effect, terms $\xi_{range}/(1-R)$ in Eq. (33) and $\xi_i/(1-R)$ in Eq. (34) were also plotted against the delamination length in Fig. 10.

3.2.2. Numerical verification

The influence of vibration-induced dynamic effect is very small (Fig. 10) and can be neglected for the test frequency of 5 Hz. Still, the developed theory (Section 2.2.2) shows that the dynamic effect increases with increasing applied frequency, and that the dynamic effect

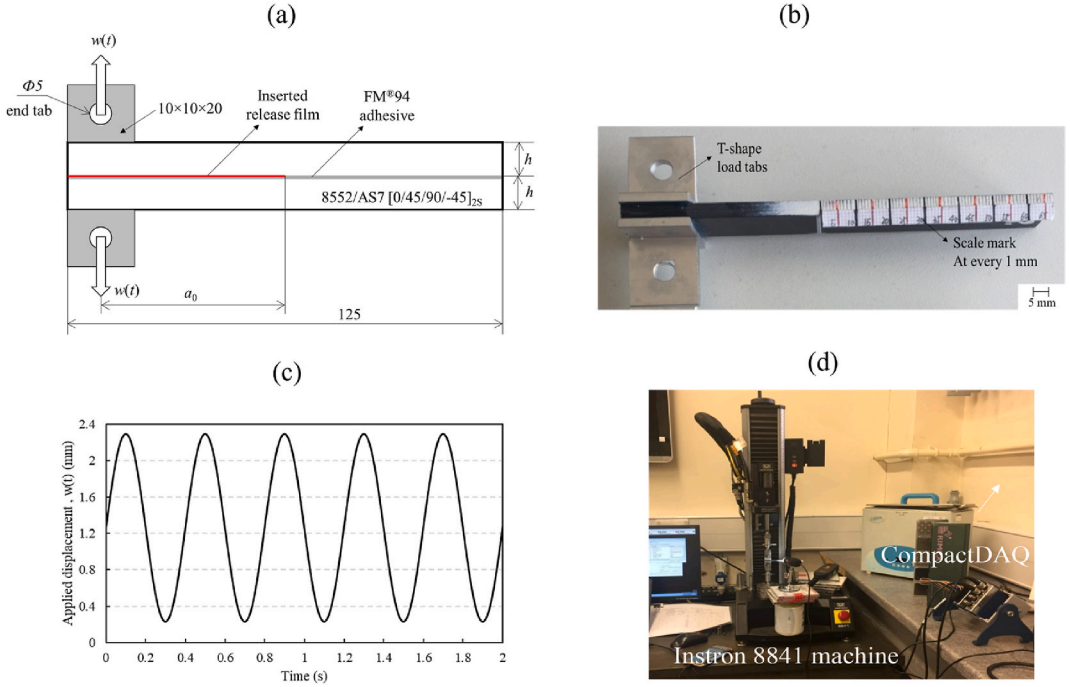

Fig. 8. (a) DCB specimen (units: mm); (b) specimen with end tabs and markings; (c) applied cyclic displacement; (d) setup for fatigue test.

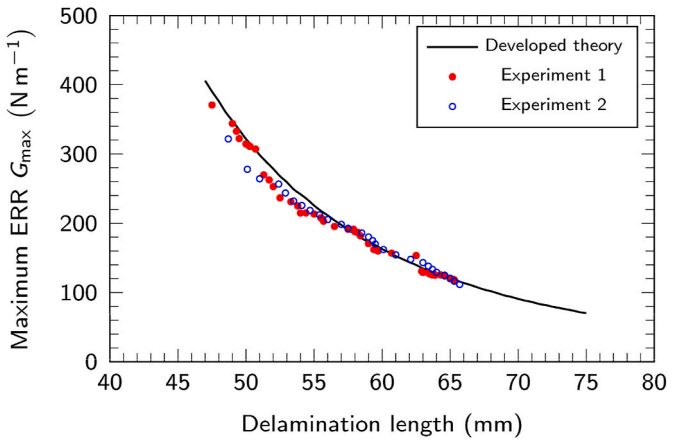

Fig. 9. Dynamic mode-I ERR versus delamination length under maximum displacement $\delta_{max} = 2.3$ mm ($R = 0.1$, $f = 5$ Hz).

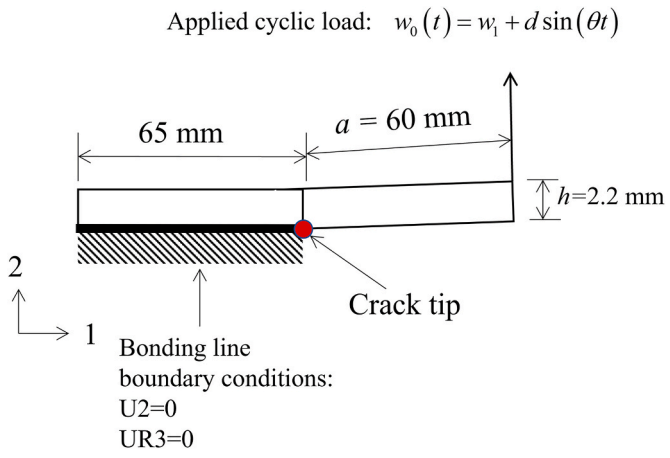

Fig. 11. Schematic of finite-element model and boundary conditions.

can become significant. Note that, to apply higher frequencies, Maillet et al. [27] designed a mechanical device capable of applying cyclic frequency up to 100 Hz. To demonstrate the applicability of the theory in Section 2.2.2 and to investigate the induced dynamic effect, the FEM was employed using a 2D model in Abaqus/Explicit with plane-strain elements (CPE4R). Mechanical properties of 8552/AS7 laminate were employed in the finite-element model according to an orthotropic elastic constitutive formulation in terms of engineering constants: $E_1 = E_2 = 56.42$ GPa, $E_3 = 10$ GPa, $G_{13} = G_{23} = 10$ GPa, $G_{12} = 21.64$ GPa, $\nu_{12} = \nu_{23} = \nu_{13} = 0.30$. Due to the symmetry, one DCB arm was modelled with the boundary conditions and applied displacement shown in Fig. 11. Small displacements were assumed. The mesh-convergence study was conducted for uniform meshes of 1×1 mm^2, 0.5×0.5 mm^2, 0.25×0.25 mm^2 and 0.125×0.125 mm^2, as shown in Fig. C1 in Appendix C, and the mesh of 0.25×0.25 mm^2 was chosen.

For a uniform mesh of 0.25×0.25 mm^2, the ERR was determined with the virtual crack-closure technique (VCCT). For test frequency of 100 Hz and delamination length 60 mm, a comparison of the analytical solution (Eq. (31)) and FEM are shown in Fig. 12a in terms of ERR-time response.

An excellent agreement between the analytical solution and FEM is obvious in Fig. 12a, confirming that the induced vibration-related dynamic effect is significant for the frequency of 100 Hz. A further examination of the ERR components in Fig. 12b using Eqs. (36)–(38) demonstrates the absolute value of dynamic component with the maximum value of 47.25 N m^{-1} and the applied ERR component of 156.21 N m^{-1}, giving a dynamic factor $f_{dyn} = 30.24\%$ according to Eq. (39). Therefore, the dynamic effect cannot be neglected.

In addition, the agreement between the developed theory and FEM simulation can be demonstrated by FFT analysis (Fig. 13). It is seen that first vibration mode makes the highest contribution to the total ERR. For the first three vibration modes, the frequencies are predicted accurately with the developed theory; quantitative comparison is given in Table 2.

It is seen that the error (relative difference) for amplitude of first vibration mode predicted with the analytical solution and FEM result is −2.53%, although the respective values for the second and third vibration modes are larger.

To further study the test frequency effect, G_{max} for the above case was calculated across a frequency range between 1 Hz and 100 Hz (Fig. 14). Evidently, the maximum applied ERR $G_{appl,max}$ (Eq. (37)) does not increase with the test frequency (Fig. 14a), but the maximum induced dynamic component $G_{dyn,max}$ increases steadily with growing frequency.

The maximum dynamic factor calculated using Eq. (39) reaches the maximum value up to 34.5% in the studied frequency range (Fig. 14b), suggesting that the induced vibration-related dynamic effect must be taken into consideration when conducting high-frequency fatigue tests.

The verification with the FEM demonstrates the accuracy of the developed theory; hence, it can be used in both low- and high-frequency fatigue delamination. Additionally, the developed theory does not require measurement of the applied loads as the conventional method (ASTM D6115) requests; this is particularly attractive for higher-frequency tests, where the applied force cannot be measured

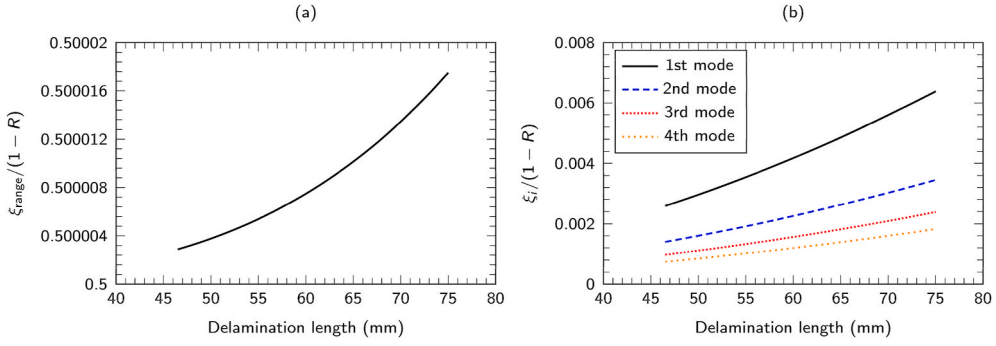

Fig. 10. (a) Contribution to total ERR from applied cyclic loads; (b) contribution to total ERR for induced vibration.

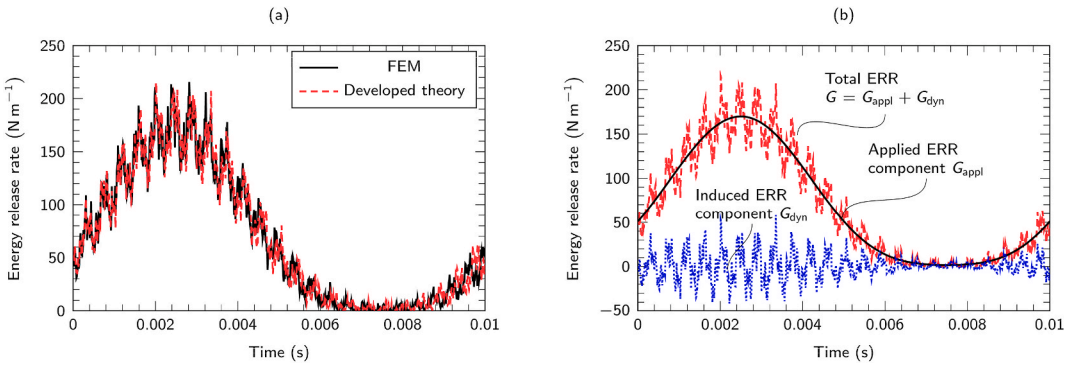

Fig. 12. (a) Comparison between developed theory and FEM; (b) partition of total ERR into applied and vibration-induced ERR components (test frequency 100 Hz).

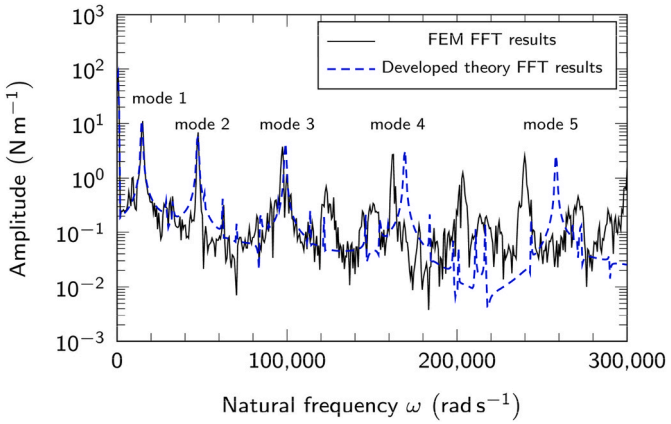

Fig. 13. Comparison of FFT results for FEM method and develop theory for first five vibration modes.

Table 2
Comparison of modal amplitudes and frequencies for FEM and developed theory.

	Amplitude (N m^{-1})			Frequency (rad s^{-1})		
	FEM	Analytical	Error (%)	FEM	Analytical	Error (%)
Mode 1	11.06	11.34	−2.53	15064.58	14436.89	4.17
Mode 2	6.86	5.01	26.97	47704.50	47076.81	1.32
Mode 3	3.73	4.35	−16.62	97292.08	99175.15	−1.94
Mode 4	2.70	3.14	−16.30	162571.93	169476.53	−4.25
Mode 5	2.53	2.60	−2.77	239777.90	257980.94	−7.59

accurately because of the significant structural vibration.

4. Conclusion

The total dynamic energy release rate (ERR) in the double cantilever beam (DCB) test under general applied displacement was derived analytically for the first time based on the structural vibration theory, allowing determination of the total ERR without measurement of the external force for arbitrary applied displacements. Two useful solutions are derived for two experimental techniques broadly used in analysis of composites: the split Hopkinson bar impact for assessment of the loading-rate effect on the delamination behavior and the cyclic loads for studying the fatigue delamination behavior.

For the DCB under Hopkinson bar impact, the total dynamic ERR can be derived and decomposed into the quasi-static and induced vibration-related components accounting for the total dynamic effect. A dynamic factor is defined for quantitative evaluation of the dynamic effect. The analytical solution was validated with the published experimental data showing an excellent agreement. The study also demonstrated the oscillating nature of the ERR caused by the opening and closing of the crack tip due to structural vibration.

For the DCB under cyclic loads, the total dynamic ERR can be decomposed into the applied ERR and vibration-induced components, and the relative dynamic effect and the total dynamic effects were defined. The analytical solution was validated by in-house fatigue delamination experiment with an excellent agreement until the crack initiation. The applicability for high-frequency cyclic loads was verified with the finite element method. It was found the that dynamic effect increased with applied load frequency, and for a particular case of 100 Hz, the dynamic effect contributed up to 34.5% of the applied ERR, showing the significance of structural vibration.

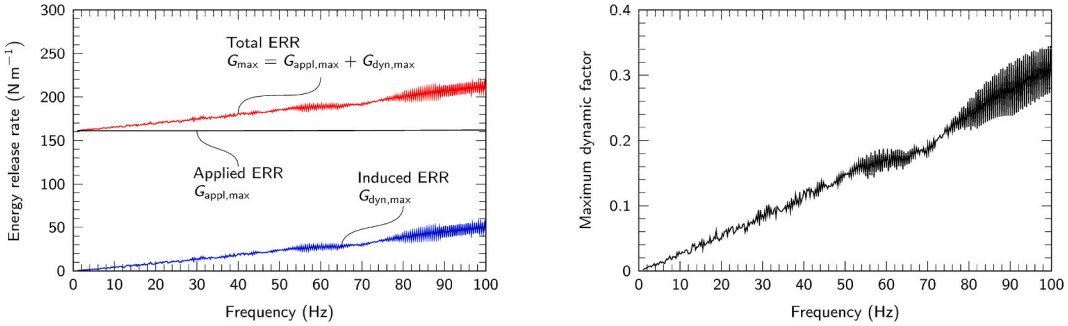

Fig. 14. (a) Total ERR and its two components obtained at maximum applied displacement; (b) dynamic factor at maximum applied displacement.

The derived theory is readily applicable to various problems for evaluation of the dynamic mode-I delamination driving force with two immediate applications for measuring the dynamic fracture toughness and determining the fatigue-delamination-deriving force as demonstrated in this study.

Data availability

The authors confirm that the data supporting the findings of this study are available within the article.

Author contributions

Tianyu Chen: Conceptualization, Methodology, Formal analysis, Writing-Original Draft, **Yiding Liu:** Conceptualization, Validation, Investigation, Data Curation, **Christopher M. Harvey:** Methodology, Formal analysis, Writing-Review&Editing, **Kun Zhang:** Visualization, Resources, Funding acquisition, Writing-Original Draft, **Simon Wang:** Methodology, Visualization, Writing-Review&Editing, **Vadim V. Silberschmidt:** Writing-Review&Editing, Supervision, **Bingchen Wei:** Project administration, Resources, Funding acquisition, **Xiang Zhang:** Visualization, Supervision, Writing-Review&Editing, All authors have read and agreed to the published version of the manuscript.

Declaration of competing interest

The authors declare that they have no known competing financial interests or personal relationships that could have appeared to influence the work reported in this paper.

Acknowledgement

This work was supported by the National Natural Science Foundation of China (Grant No. 51401028, No. 51271193, No. 11790292), the Strategic Priority Research Program of the Chinese Academy of Sciences (Grant No. XDB22040303), and the Innovation Program (23709900000170004).

Appendices.

Appendix A. Boundary conditions

The boundary conditions for the free-vibration component $w_{\mathrm{fv}}(x,t)$ and the shifting functions $F_n(x)$ and $H_m(x)$ are presented in Table A1.

Table A.1
Boundary conditions for $w(x,t)$ and its components

Boundary	Total deflection $w(x,t)$	Free-vibration component $w_{\mathrm{fv}}(x,t)$	Mode shape $\varphi_i(x)$	Shifting functions $F_n(x)$		Shifting functions $H_m(x)$
				$n=0$	$n\geq 1$	
$x=0$	$w(0,t)=0$	$w_{\mathrm{fv}}(0,t)=0$	$\varphi_i(0)=0$	$F_0(0)=0$	$F_n(0)=0$	$H_m(0)=0$
	$w^{(1)}(0,t)=0$	$w_{\mathrm{fv}}^{(1)}(0,t)=0$	$\varphi_i^{(1)}(0)=0$	$F_0^{(1)}(0)=0$	$F_n^{(1)}(0)=0$	$H_m^{(1)}(0)=0$
$x=a$	$w(a,t)=w_0(t)$	$w_{\mathrm{fv}}(a,t)=0$	$\varphi_i(a)=0$	$F_0(a)=0$	$F_n(a)=1$	$H_m(a)=1$
	$w^{(2)}(a,t)=0$	$w_{\mathrm{fv}}^{(2)}(a,t)=0$	$\varphi_i^{(2)}(a)=0$	$F_0^{(2)}(a)=0$	$F_n^{(2)}(a)=0$	$H_m^{(2)}(a)=0$

Appendix B. Solution for frequency equation and relevant modal parameters

Table B.1
Solution of frequency equation and relevant modal parameters

Mode number	λ_i	σ_i	Λ_i
1	3.92660231	1.000777304	−1.375327127
2	7.06858275	1.000001445	1.415914585
3	10.21017612	1.000000000	$-\sqrt{2}$
4	13.35176878	1.000000000	$\sqrt{2}$
5	16.49336143	1.000000000	$-\sqrt{2}$
$i>5$	$(4i+1)\pi/4$	1.0	$(-1)^i\sqrt{2}$

Appendix C. Results of mesh-size convergence study

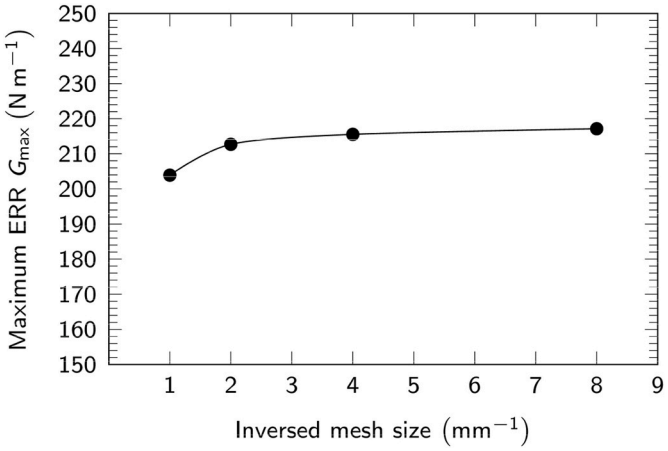

Fig. C1. Mesh-size convergence results

Supplementary data

Supplementary data to this article can be found online at https://doi.org/10.1016/j.compscitech.2022.109632.

References

[1] C. Soutis, Carbon fiber reinforced plastics in aircraft construction, Mater. Sci. Eng., A 412 (1–2) (2005) 171–176, https://doi.org/10.1016/J.MSEA.2005.08.064.

[2] C. González, J.J. Vilatela, J.M. Molina-Aldareguía, C.S. Lopes, J. LLorca, Structural composites for multifunctional applications: current challenges and future trends, Prog. Mater. Sci. 89 (2017) 194–251.

[3] T.A. Sebaey, N. Blanco, J. Costa, C.S. Lopes, Characterization of crack propagation in mode I delamination of multidirectional CFRP laminates, Compos. Sci. Technol. 72 (11) (2012) 1251–1256.

[4] S. Ogihara, N. Takeda, Interaction between transverse cracks and delamination during damage progress in CFRP cross-ply laminates, Compos. Sci. Technol. 54 (4) (1995) 395–404.

[5] M.R. Wisnom, The role of delamination in failure of fibre-reinforced composites, Philos. Trans. R. Soc. A Math. Phys. Eng. Sci. 370 (1965) (2012) 1850–1870.

[6] X. Zhao, W. Chen, X. Han, Y. Zhao, S. Du, Enhancement of interlaminar fracture toughness in textile-reinforced epoxy composites with polyamide 6/graphene oxide interlaminar toughening tackifier, Compos. Sci. Technol. 191 (2020), 108094.

[7] J. Zhang, T. Yang, T. Lin, C.H. Wang, Phase morphology of nanofibre interlayers: critical factor for toughening carbon/epoxy composites, Compos. Sci. Technol. 72 (2) (2012) 256–262.

[8] X. Sun, L. Tong, M.D.K. Wood, Y.W. Mai, Effect of stitch distribution on mode I delamination toughness of laminated DCB specimens, Compos. Sci. Technol. 64 (7–8) (2004) 967–981.

[9] T. Yang, C.H. Wang, J. Zhang, S. He, A.P. Mouritz, Toughening and self-healing of epoxy matrix laminates using mendable polymer stitching, Compos. Sci. Technol. 72 (12) (2012) 1396–1401.

[10] B. M'membe, M. Yasaee, S.R. Hallett, I.K. Partridge, Effective use of metallic Z-pins for composites' through-thickness reinforcement, Compos. Sci. Technol. 175 (2018) (2019) 77–84.

[11] S. Tang, S. Lemanski, X. Zhang, D. Ayre, Fatigue life prediction of z-fibre pinned composite laminate under mode I loading, Compos. Sci. Technol. 174 (2019) 221–231.

[12] ASTM D5528, Standard Test Method for Mode I Interlaminar Fracture Toughness of Unidirectional Fiber-Reinforced Polymer Matrix Composites, ASTM International, 2014.

[13] M. May, Measuring the rate-dependent mode I fracture toughness of composites - a review, Compos. Part A Appl. Sci. Manuf. 81 (2016) 1–12.

[14] L.B. Freund, Dynamic Fracture Mechanics, Cambridge University Press, 1990.

[15] T. Chen, C.M. Harvey, S. Wang, V.V. Silberschmidt, Dynamic interfacial fracture of a double cantilever beam, Eng. Fract. Mech. 225 (2020) 1–9.

[16] T. Chen, C.M. Harvey, S. Wang, V.V. Silberschmidt, Delamination propagation under high loading rate, Compos. Struct. 253 (2020), 112734.

[17] T. Chen, C.M. Harvey, S. Wang, V.V. Silberschmidt, Dynamic delamination on elastic interface, Compos. Struct. 234 (2020), 111670.

[18] G. Hug, P. Thévenet, J. Fitoussi, D. Baptiste, Effect of the loading rate on mode I interlaminar fracture toughness of laminated composites, Eng. Fract. Mech. 73 (16) (2006) 2456–2462.

[19] M. Colin de Verdiere, A.A. Skordos, A.C. Walton, M. May, Influence of loading rate on the delamination response of untufted and tufted carbon epoxy non-crimp fabric composites/Mode II, Eng. Fract. Mech. 96 (2012) 1–10.

[20] C. Sun, C. Han, A method for testing interlaminar dynamic fracture toughness of polymeric composites, Compos. B Eng. 35 (6–8) (2004) 647–655.

[21] H. Liu, H. Nie, C. Zhang, Y. Li, Loading rate dependency of Mode I interlaminar fracture toughness for unidirectional composite laminates, Compos. Sci. Technol. 167 (2018) 215–223.

[22] C. Guo, C.T. Sun, Dynamic mode-I crack-propagation in a carbon/epoxy composite, Compos. Sci. Technol. 58 (9) (1998) 1405–1410.

[23] P. Kumar, N.N. Kishore, Initiation and propagation toughness of delamination crack under an impact load, J. Mech. Phys. Solid. 46 (10) (1998) 1773–1787.

[24] D.6115 ASTM, Standard Test Method for Mode I Fatigue Delamination Growth Onset of Unidirectional, ASTM International, 2005.

[25] M. Hojo, S. Matsuda, M. Tanaka, S. Ochiai, A. Murakami, Mode I delamination fatigue properties of interlayer-toughened CF/epoxy laminates, Compos. Sci. Technol. 66 (5) (2006) 665–675.

[26] Y. Liu, X. Zhang, S. Lemanski, H.Y. Nezhad, D. Ayre, Experimental and numerical study of process-induced defects and their effect on fatigue debonding in composite joints, Int. J. Fatig. 125 (2019) 47–57.

[27] I. Maillet, L. Michel, G. Rico, M. Fressinet, Y. Gourinat, A new test methodology based on structural resonance for mode I fatigue delamination growth in an unidirectional composite, Compos. Struct. 97 (2013) 353–362.

[28] C.S. Lee, H.J. Kim, A. Amanov, J.H. Choo, Y.K. Kim, I.S. Cho, Investigation on very high cycle fatigue of PA66-GF30 GFRP based on fiber orientation, Compos. Sci. Technol. 180 (2019) 94–100.

[29] D. Backe, F. Balle, D. Eifler, Fatigue testing of CFRP in the very high cycle fatigue (VHCF) regime at ultrasonic frequencies, Compos. Sci. Technol. 106 (2015) 93–99.

[30] S. Hashemi, A.J. Kinloch, J.G. Williams, Corrections needed in double-cantilever beam tests for assessing the interlaminar failure of fibre-composites, J. Mater. Sci. Lett. 8 (2) (1989) 125–129.

[31] T. Chen, C.M. Harvey, S. Wang, V.V. Silberschmidt, Analytical corrections for double-cantilever beam tests, Int. J. Fract. 229 (2) (2021) 269–276.

[32] D.A. Grant, Beam vibrations with time-dependent boundary conditions, J. Sound Vib. 89 (4) (1983) 519–522.

[33] S.S. Rao, Vibration of Continuous Systems, John Wiley & Sons, 2007.

[34] R.D. Blevins, Formulas for Natural Frequency and Mode Shape, Van Nostrand Reinhold, 1979.